

Article

Pyridine-2,6-Dicarboxylic Acid Esters (pydicR₂) as O,N,O-Pincer Ligands in Cu^{II} Complexes

Katharina Butsch ¹, Aaron Sandleben ¹ , Maryam Heydari Dokoohaki ², Amin Reza Zolghadr ^{2,*} and Axel Klein ^{1,2,*} 

¹ Department für Chemie, Institut für Anorganische Chemie, Universität zu Köln, Greinstraße 6, D-50939 Köln, Germany; Katharinabutsch@web.de (K.B.); a.sandleben@uni-koeln.de (A.S.)

² Chemistry Department Faculty of Science, Shiraz University, Shiraz 71454, Iran; maryamhdi5844@gmail.com

* Correspondence: arzolghadr@shirazu.ac.ir (A.R.Z.); axel.klein@uni-koeln.de (A.K.); Tel.: +49-221-470-4006 (A.K.)

Received: 15 February 2019; Accepted: 9 April 2019; Published: 14 April 2019

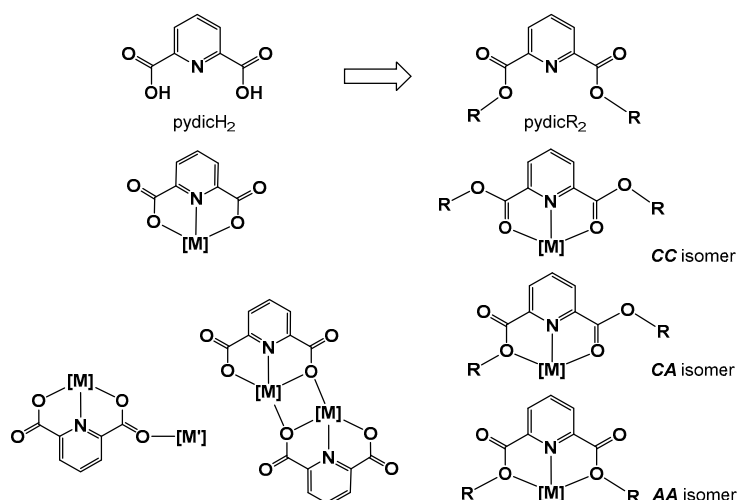


Abstract: The pyridine-2,6-carboxylic esters pydicR₂ with R = Me or Ph form the unprecedented mononuclear Cu^{II} complexes [Cu(pydicR₂)Cl₃][−] in one-pot reactions starting from pyridine-2,6-carboxychloride pydicCl₂, Cu^{II} chloride, and NEt₃ in MeOH or PhOH solution under non-aqueous conditions. The triethylammonium salts (HNEt₃)[Cu(pydicR₂)Cl₃] were isolated. The methyl derivative could be crystallized to allow a XRD structure determination. Both structures were optimized using DFT calculations in various surroundings ranging from gas phase and the non-coordinating solvent CH₂Cl₂ to the weakly coordinating acetone and well-coordinating solvents acetonitrile (MeCN) or dimethylformamide (DMF), while detailed calculation showed the charge distribution, dipole moments, and HOMO–LUMO gap energies changing upon solvation. According to these calculations, the ion pairs and the anionic Cu^{II} complexes were stable, which shows only Cu–Cl bond elongation and weakening of the charge transfer between the anionic complex and the cation as solvents become polar. Synthesis attempts in the presence of water yielded the Cu^{II} complexes [Cu(pydic)(OH₂)₂]_n and [Cu(OH₂)₆][{Cu(pydic)}₂(μ-Cl)₂], which results from pydicCl₂ hydrolysis. Alternatively, the new pydic(IPh)₂ (IPh = 2-iodo-phenyl) ester ligand was synthesized and reacted with anhydrous CuCl₂, which yields the new binuclear complex [{Cu(pydic(IPh)₂)Cl₂(μ-Cl)₂}. EPR spectroscopy of the solid compounds reveals typical axial spectra in line with the observed and DFT calculated geometries. Cyclic voltammetry and UV–vis absorption spectroscopy in solution are in line with un-dissociated complex species [Cu(pydicR₂)Cl₃][−].

Keywords: oxido-pincer ligands; Cu^{II}; DFT calculations; EPR spectroscopy; electrochemistry

1. Introduction

Pyridine-2,6-dicarboxylic esters are interesting oxido pincer ligands with an O,N,O donor set. They are derived from the potentially O,N,O tridentate binding 2,6-dicarboxylic acid (pydicH₂) (Scheme 1). Pyridine-2,6-dicarboxylate (pydic^{2−}) is a frequently used ligand and coordinates are usually in a deprotonated tridentate mode. The coordinates use the N donor atom and the two carboxylate O donor functions, including the possibility of bridging (Scheme 1) [1–14]. In contrast to this, the pydic ester ligands are neutral and have three options of tris-chelate O,N,O binding, which gives rise to three different isomers O_{carbonyl}–M–O_{carbonyl} (CC isomer), O_{carbonyl}–M–O_{alkoxy} (CA isomer), and O_{alkoxy}–M–O_{alkoxy} (AA isomer) (Scheme 1) while a bridging mode observed frequently for pydic^{2−} is less probable [15–17].



Scheme 1. Binding modes of pydic²⁻ compared to pyridine-2,6-dicarboxylic ester ligands (R = alkyl or aryl; [M] = metal ions or metal complex fragments).

Pyridine-2,6-dicarboxylic alkyl- or arylester derivatives pydicR₂ coordinating to metal ions have been reported with R = methyl [15–21], ethyl [18,20,22–26], *iso*-propyl [18], *n*-butyl [26], and benzyl [18], with further complexes containing related non-symmetric or macrocyclic esters RpydicR' [23,24,27–30]. Aryl substituted systems are less frequent [27]. In most of these examples, the ligands coordinate in a tridentate mode. However, bidentate N,O coordination or monodentate N coordination has been observed [15,16,20,21,28]. Recently, Hakimi et al. found in the Cambridge Crystallographic Database that, from the complexes showing tridentate O,N,O coordination, roughly 42% of the submitted structures show O_{carbonyl}–M–O_{carbonyl} coordination (CC isomers, Scheme 1) [15], while AA (O_{alkoxy}–M–O_{alkoxy}) and CA (O_{carbonyl}–M–O_{alkoxy}) isomers make up about 29% each. The CC isomers are expected to be superior to the CA and AA isomers since the carbonyl function provides less steric strain and potentially π back-bonding options in addition to the σ coordination of the O lone pairs. Quite generally, both O_{carbonyl} and O_{alkoxy} coordination is considered to be relatively weak, e.g., compared to the carboxylate ligand function of pydic²⁻. Ester functions in polydentate ligands have been applied as hemilabile ligand functions in catalysis [31–35].

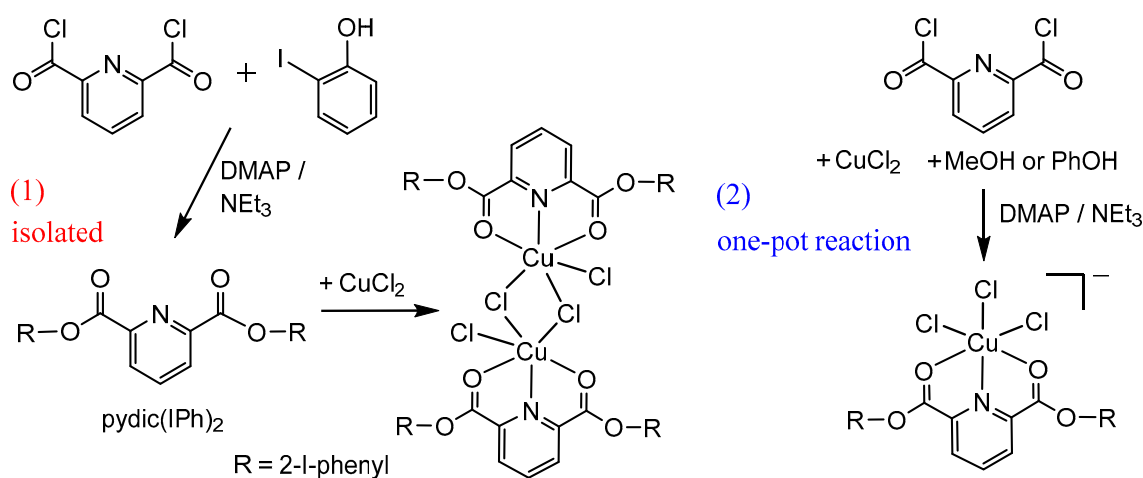
In this contribution, we will report on our investigations about the coordination of Cu^{II} toward the pyridine-2,6-dicarboxylic ester pydicR₂ ligands with R = Me, Ph, and 2-iodo-phenyl (IPh). We report their synthesis and compare their molecular structures in the solid using single crystal XRD with the structures under various environments (gas phase, solution) using quantum chemical calculations based on the density functional theory (DFT). In these calculations, we were probing for their structural variability in terms of isomers, ion pair stabilization, or ligand replacement by potentially coordinating solvents such as MeCN and DMF. Detailed DFT calculations also revealed the influence of increasing solvent polarity on the dipole moments and charge distribution in the ion pairs. Since Cu^{II} (d⁹, S = 1/2) provides very useful spectroscopic (d–d bands, EPR) and electrochemical (Cu^{II}/Cu^I couple) patterns to study geometries and the strength of M–ligand bonds, we added EPR spectroscopy in the solid and solution to this study, together with UV–vis absorption, cyclic voltammetry, and UV–vis spectroelectrochemistry of selected compounds in the solution.

2. Results and Discussion

2.1. Synthesis and Molecular Structures of pydicR₂ Ligands and their Cu^{II} Complexes

Two different reaction strategies were used to synthesize Cu^{II} complexes (Scheme 2). The first route has been previously used, e.g., for the formation of pydic ester complexes [(Cu(pydicR₂)Cl)₂(μ -Cl)₂]

(R = Me, Et, ⁱPr) [17,22] and consists of two subsequent steps, the synthesis of the pydicR₂ ligand, and its isolation followed by the complex formation reaction (1).



Scheme 2. Two reaction strategies to synthesize Cu^{II} complexes of pydicR₂ ligands (DMAP = dimethyl 4-aminopyridine).

This method allowed the synthesis of the new ligand pydic(IPh)₂ (IPh = 2-iodo-phenyl) in 82% yield (spectroscopic characterization, see Experimental Section). Single crystals suitable for XRD were obtained from acetone solutions by slow evaporation and the structure was solved in the orthorhombic space group *Pbca* (further details, full data, and Figure S1 in the Supplementary Materials). Reacting pydic(IPh)₂ with anhydrous CuCl₂ gave a new complex as a brown powder in 67% yield with a ligand:Cu ratio of 1:1 from elemental analysis. Similar reactions using pydicMe₂, pydicEt₂, or pydicⁱPr₂ have been reported, which yielded binuclear complexes [$\text{[Cu(pydicR}_2\text{)Cl}_2\text{]}_2(\mu\text{-Cl})_2$] [17,22,23]. We assume a binuclear structure for [$\text{[Cu(pydic(IPh)}_2\text{)Cl}_2\text{]}_2(\mu\text{-Cl})_2$]. DFT-calculated optimized geometries confirmed this with the binuclear structure being more stable by about 75 kJ/mol compared with the mononuclear [Cu(pydic(IPh)₂)Cl₂] (Figure 1). Importantly, both the mononuclear and the binuclear complex show the CC isomeric structure (Scheme 1) with the two carbonyl O atoms binding to Cu^{II} in the two markedly elongated axial positions of a distorted trigonal pyramidal (mononuclear) or pseudo-octahedral (binuclear) coordination. Comparison of the calculated coordination modes CC, CA, and AA shows that the CC isomer is energetically favored.

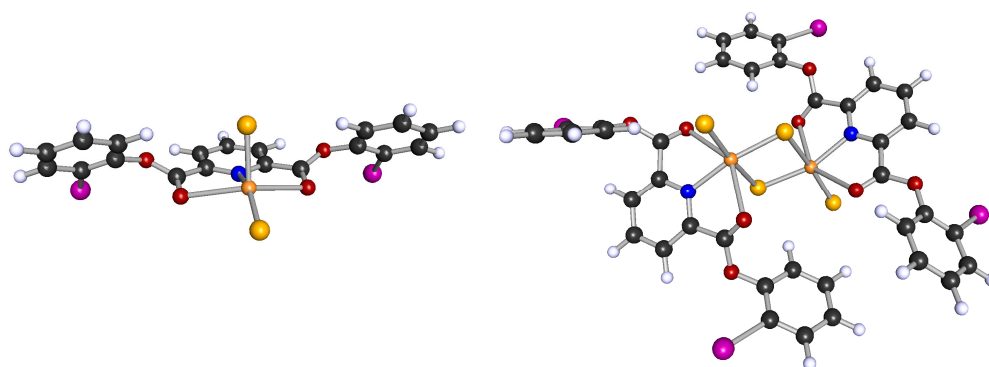


Figure 1. DFT-calculated optimized geometry of mononuclear [Cu(pydic(IPh)₂)Cl₂] (left) and binuclear [$\text{[Cu(pydic(IPh)}_2\text{)Cl}_2\text{]}_2(\mu\text{-Cl})_2$] (right). Calculated at the def-SV(P)/B3LYP level.

In addition to this, we had the idea to set up a one-pot reaction using pyridine-2,6-dicarbonyl dichloride (pydicCl₂), a Cu^{II} source, and the corresponding alcohol (methanol or phenol) to form the ligand in the presence of the coordinating metal ion and a base (2). The base was quite similar to

what has been reported recently for the formation of lanthanide coordinated IRMOF-3-PY through a post-synthetic modification [5].

In initial experiments, we reacted $\text{CuCl}_2 \cdot 2\text{H}_2\text{O}$ and not carefully dried $\text{Cu}(\text{OAc})_2$, methanol or phenol, and pydic Cl_2 in a 1:1 ratio. In low yields of 12% and 24%, respectively, we could isolate $[\text{Cu}(\text{OH}_2)_6][\{\text{Cu}(\text{pydic})_2(\mu\text{-Cl})_2\}]$ and $[\text{Cu}(\text{pydic})(\text{OH}_2)_2]_n$ (pydic $^{2-}$ = pyridine-2,6-dicarboxylate). Both compounds resulted from the hydrolysis of pydic Cl_2 to pydic $^{2-}$ in the presence of water while no ester was formed. The crystal structure (monoclinic $P2_1/c$) of $[\text{Cu}(\text{pydic})(\text{OH}_2)_2]_n$ was reported before [36,37]. XRD suitable crystals of $[\text{Cu}(\text{OH}_2)_6][\{\text{Cu}(\text{pydic})_2(\mu\text{-Cl})_2\}]$ were obtained by slow evaporation of a methanol solution. The crystal structure was solved and refined in the triclinic space group $P\bar{1}$ (Figure 2, further details and full data in the Supplementary Materials). The structure reveals the complex cation $[\text{Cu}(\text{OH}_2)_6]^{2+}$ and a centrosymmetric binuclear μ -chlorido bridged dianionic complex $[\{\text{Cu}(\text{pydic})_2(\mu\text{-Cl})_2\}]^{2-}$. $[\text{Cu}(\text{OH}_2)_6]^{2+}$ can be described as an axially elongated octahedron ($\text{Cu}2\text{-O}5 = 1.979(9)$ Å, $\text{Cu}2\text{-O}6 = 1.965(9)$ Å, and $\text{Cu}2\text{-O}11 = 2.53(2)$ Å), which is in line with previous reports [38,39]. The di-anion $[\{\text{Cu}(\text{pydic})_2(\mu\text{-Cl})_2\}]^{2-}$ shows a distorted square pyramidal geometry around each copper atom with a short equatorial bond $\text{Cu}\text{-Cl}_{\text{eq}} = 2.212(4)$ Å, long axial bond $\text{Cu}\text{-Cl}_{\text{ax}} = 2.692(3)$ Å, and a rather short equatorial $\text{Cu}\text{-N}$ bond (1.93(1) Å). Very similar bond parameters have been reported for the dianion $[\{\text{Cu}(\text{pydic})_2(\mu\text{-Cl})_2\}]^{2-}$ in the compounds $[\text{Cu}(\text{MeOH})(\text{H}_2\text{O})_4][\text{Cu}_2(\text{pydic})_2(\mu\text{-Cl})_2] \cdot \text{H}_2\text{O}$ [40] and $[\text{Cu}(\text{Pz})_2(\text{H}_2\text{O})_4][\text{Cu}_2(\text{pydic})_2(\mu\text{-Cl})_2]$ (Pz = pyrazole) [41].

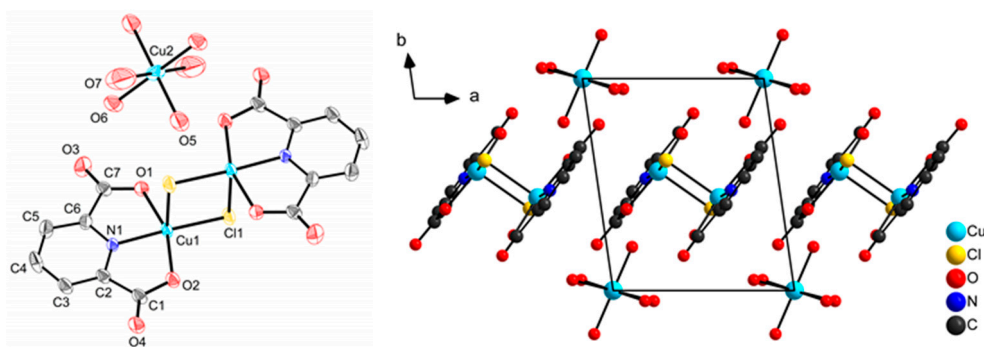


Figure 2. Left: ORTEP representation (50% probability level) of the molecular structure of $[\text{Cu}(\text{OH}_2)_6][\{\text{Cu}(\text{pydic})_2(\mu\text{-Cl})_2\}]$. H atoms were omitted for clarity. Right: Crystal structure of $[\text{Cu}(\text{OH}_2)_6][\{\text{Cu}(\text{pydic})_2(\mu\text{-Cl})_2\}]$ along the crystallographic c -axis.

In further synthesis experiments using freshly distilled starting materials and anhydrous CuCl_2 , we obtained yellow-green crystalline materials. Repeated re-crystallisation from methanol was necessary but lowered the yields to 32% and 54% of the complexes $(\text{HNEt}_3)[\text{Cu}(\text{pydicMe}_2)\text{Cl}_3]$ and $(\text{HNEt}_3)[\text{Cu}(\text{pydicPh}_2)\text{Cl}_3]$. Thus, under water-free conditions, the in situ formation of the corresponding pydicR $_2$ ligands and coordination to Cu^{II} (one-pot) is possible. Single crystals of $(\text{HNEt}_3)[\text{Cu}(\text{pydicMe}_2)\text{Cl}_3]$ were obtained from methanol solution and structure solution and refinement were carried out in the triclinic space group $P\bar{1}$ (data in the Supplementary Materials). The molecular structure is depicted in Figure 3 and shows the Cu ion in a distorted octahedral surrounding the carbonyl oxygen atoms of the O,N,O-ester binding to the copper atom (CC isomer). The three $\text{Cu}\text{-Cl}$ bonds with 2.306(2) Å, 2.255(2) Å, and 2.306(2) Å and the $\text{Cu}\text{-N}1$ bond of 2.065(4) Å define a distorted square plane. The two $\text{Cu}\text{-O}$ bonds $\text{Cu}\text{-O}2 = 2.503(4)$ Å and $\text{Cu}\text{-O}4 = 2.551(3)$ Å are non-equivalent and represent the long bonds of an axially elongated pseudo-octahedron. The real local symmetry at the Cu atom can be idealized as C_{2v} . Two strong hydrogen bonds [42] are formed between the triethyl ammonium ion and two chlorido ligands of the complex anion ($\text{H}22 \cdots \text{Cl}1 = 2.70(4)$ Å and $\text{H}22 \cdots \text{Cl}2 = 2.48(4)$ Å, $\text{Cl}1 \cdots \text{H}22 \cdots \text{Cl}2 = 79(1)^\circ$).

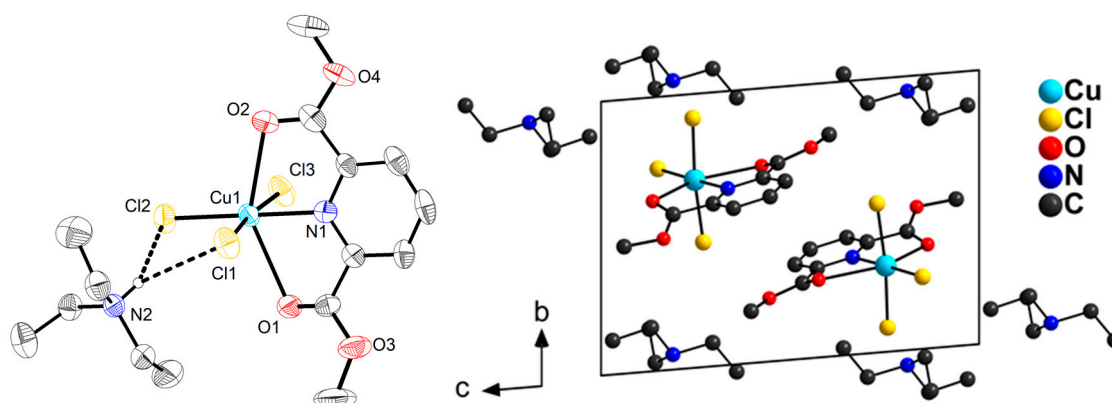


Figure 3. ORTEP representation (50% probability level) of the molecular structure of $(\text{HNEt}_3)[\text{Cu}(\text{pydicMe}_2)\text{Cl}_3]$. H atoms are omitted for clarity. Right: Crystal structure of $(\text{HNEt}_3)[\text{Cu}(\text{pydicMe}_2)\text{Cl}_3]$ along the crystallographic a -axis.

Comparison of $(\text{HNEt}_3)[\text{Cu}(\text{pydicMe}_2)\text{Cl}_3]$ with the reported complex $[\text{Cu}(\text{pydicMe}_2)(\text{H}_2\text{O})_3](\text{ClO}_4)_2$ [17] reveals the same bond parameters within the pydicMe₂ ligand, similar Cu–ligand distances in the equatorial plane: Cu–N 1.990(3) Å, Cu–OH₂ 1.992(3), 1.949(3), and 2.000(3) Å, respectively, and long Cu–O_{keto} bonds of 2.332(3) and 2.338(3) Å. Thus, both Cl[−] in $[\text{Cu}(\text{pydicMe}_2)\text{Cl}_3]$ and H₂O in $[\text{Cu}(\text{pydicMe}_2)(\text{H}_2\text{O})_3]$ represent stronger ligands than the carbonyl ester O atoms.

2.2. DFT Calculations on the Solvation of $(\text{HNEt}_3)[\text{Cu}(\text{pydicR}_2)\text{Cl}_3]$ ($R = \text{Me}$ or Ph)

To achieve insight into the electronic structure of the compounds, density functional theory (DFT) calculations in the gas phase and various solvent environments are performed (B3LYP/6–31+G(d,p) using Gaussian). The Cu atom was treated using LANL2DZ relativistic pseudo potentials. The final optimized geometry of the compounds in the gas phase is depicted in Figure 4. The calculated C_{2v} -symmetric structure of the ion pair $(\text{HNEt}_3)^+ \cdots [\text{Cu}(\text{pydicMe}_2)\text{Cl}_3]^-$ in the gas phase is very similar to the crystal structure, e.g., with two strong hydrogen bonds N2–H22 \cdots Cl1 (2.98 Å) and N2–H22 \cdots Cl2 (2.01 Å).

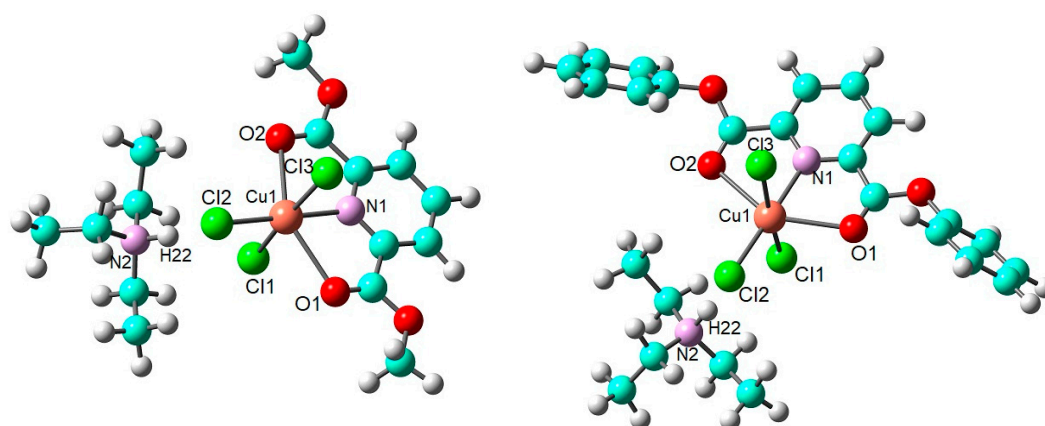


Figure 4. DFT-calculated geometry-optimized (B3LYP/6–31+G(d,p), Gaussian) structures of $(\text{HNEt}_3)[\text{Cu}(\text{pydicMe}_2)\text{Cl}_3]$ and $(\text{HNEt}_3)[\text{Cu}(\text{pydicPh}_2)\text{Cl}_3]$ in the gas phase with numbering.

In CH_2Cl_2 , acetone, DMF, and MeCN solution, the geometry of the complexes remains rather intact. Only the Cu–Cl₃ bond is markedly elongated with a slight tendency of longer bonds for more polar solvents along this series. Even more pronounced is the increasing distance between the ions due to the shielding of electrostatic interactions in these solutions (see Tables S3–S7 in the Supplementary Materials). The computed dipole moments of the complexes are significantly increased in solution

compared with the gas phase (Table 1) and the electric permittivity of the solvents clearly has a very pronounced effect on the dipole moments, even in CH_2Cl_2 . In order to investigate the solubility and thermodynamic stability of $(\text{HNEt}_3)[\text{Cu}(\text{pydicR}_2)\text{Cl}_3]$ in the surrounding medium, the solvation energies are calculated. The solvation energy of the system is determined by calculating the free energy differences in the solvent and the gas phase (Table 1). The solvation energies vary from about -110.88 to -135.12 kJ/mol and increase together with the dipole moment of the complex when increasing the electric permittivity of the solvents. Negative values of solvation energies denote that solvation of these complexes is spontaneous. To get an idea about the kinetic stability and chemical reactivity of these complexes, we also calculated the difference between the highest occupied molecular orbital (HOMO) and the lowest unoccupied molecular orbital (LUMO) ($E_{\text{LUMO}} - E_{\text{HOMO}}$) for the complexes in each solvent (Table 1). The spatial distributions of HOMO, SOMO, and LUMO of the complexes are supplied in the Supplementary Materials (Figure S8). In general, molecules with a small energy gap are more polarizable [43] and will have higher chemical activity and lower kinetic stability [44]. Overall, the HOMO–LUMO gap decreases as the electric permittivity of the solvents declines along the series DMF ($\epsilon = 37.22$) > MeCN ($\epsilon = 35.69$) >> acetone ($\epsilon = 20.49$) >> CH_2Cl_2 ($\epsilon = 8.93$). However, the absolute values are quite similar for all four solvents, which means that a pronounced activation by the polar solvents DMF or MeCN compared with acetone or CH_2Cl_2 seems not to be the case.

Table 1. DFT-calculated dipole moments and solvation energies of $(\text{HNEt}_3)[\text{Cu}(\text{pydicMe}_2)\text{Cl}_3]$ and $(\text{HNEt}_3)[\text{Cu}(\text{pydicPh}_2)\text{Cl}_3]$ in the gas phase and solvent media.

Compound		Gas Phase	CH_2Cl_2	Acetone	MeCN	DMF
$(\text{HNEt}_3)[\text{Cu}(\text{pydicMe}_2)\text{Cl}_3]$	dipole moment (Debye)	8.27	12.49	13.22	13.49	13.51
	solvation energy (kJ/mol)		-110.88	-128.30	-134.74	-135.12
	$E_{\text{LUMO}} - E_{\text{HOMO}}$ (kJ/mol)	323.15	382.64	390.20	392.91	393.06
	charge $[\text{Cu}(\text{pydicMe}_2)\text{Cl}_3]^-$	-0.84006	-0.90691	-0.91645	-0.91969	-0.92005
$(\text{HNEt}_3)[\text{Cu}(\text{pydicPh}_2)\text{Cl}_3]$	dipole moment (Debye)	7.97	12.29	13.13	13.44	13.46
	solvation energy (kJ/mol)		-124.86	-139.25	-146.15	-146.55
	$E_{\text{LUMO}} - E_{\text{HOMO}}$ (kJ/mol)	314.22	369.83	376.68	379.41	379.57
	charge					
	$[\text{Cu}(\text{pydicPh}_2)\text{Cl}_3]^-$	-0.84929	-0.90889	-0.92116	-0.92426	-0.92447

The electron density of $(\text{HNEt}_3)[\text{Cu}(\text{pydicMe}_2)\text{Cl}_3]$ and $(\text{HNEt}_3)[\text{Cu}(\text{pydicPh}_2)\text{Cl}_3]$ in the gas phase can be visualized from the three-dimensional electrostatic potential map (EPM) surfaces (Figure 5). The distribution of negative and positive charges within the EPM surfaces are depicted by red and blue colors, respectively. As a result of change in electron densities in EPM surfaces upon solvation, the charges of the anions and cations both decrease along the series. $\text{DMF} > \text{MeCN} > \text{acetone} > \text{CH}_2\text{Cl}_2 >> \text{gas phase}$ (Table 1, Figures S9 and S10 in the Supplementary Materials).

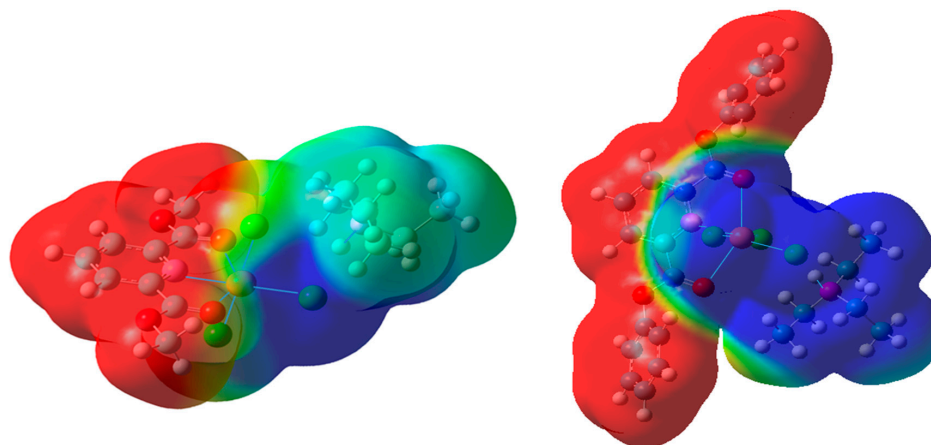


Figure 5. Electrostatic potential maps of $(\text{HNEt}_3)[\text{Cu}(\text{pydicMe}_2)\text{Cl}_3]$ (left) and $(\text{HNEt}_3)[\text{Cu}(\text{pydicPh}_2)\text{Cl}_3]$ (right) in the gas phase. Contours are color-coded from red (negative) to blue (positive).

To better understand the inclusion of the solvent effect on the DFT calculations and also the nature of interactions in the $(\text{HNEt}_3)[\text{Cu}(\text{pydicR}_2)\text{Cl}_3]$ compounds, natural bond orbital (NBO) analyses were carried out as implemented in the Gaussian program package. In the NBO analysis, the donor and acceptor interaction energies can be estimated through the second-order perturbation theory, which is described by the equation below.

$$E^{(2)} = q_i \frac{F(i,j)^2}{\varepsilon_i - \varepsilon_j}$$

where q_i is the donor orbital occupancy, ε_j and ε_i are diagonal elements, and $F(i,j)$ is the off-diagonal NBO Fock matrix element. The most important donor-acceptor interactions with high second-order perturbation energies $E^{(2)}$ are provided in Table 2 (data for the pydicPh derivative in Table S8 in the Supplementary Materials).

Table 2. DFT-calculated second-order perturbation energies $E^{(2)}$ (kJ/mol) of selected orbital interactions in $(\text{HNEt}_3)[\text{Cu}(\text{pydicMe}_2)\text{Cl}_3]$ in the gas phase and solvents ^a.

Donor	Acceptor	Gas Phase	CH ₂ Cl ₂	Acetone	MeCN	DMF
LP*(8) Cu1	BD*(1) N2–H22	18.91	8.24	7.28	6.95	6.90
LP(1) Cl1	LP*(7) Cu1	48.53	50.54	51.21	51.42	51.46
LP(4) Cl1	LP*(6) Cu1	99.62	98.78	99.29	99.54	99.54
LP(4) Cl1	LP*(7) Cu1	167.40	179.53	181.21	181.84	181.88
LP(1) Cl2	LP*(8) Cu1	61.30	57.91	57.74	57.61	57.70
LP(4) Cl2	LP*(6) Cu1	107.15	126.40	128.37	128.99	129.04
LP(4) Cl2	LP*(8) Cu1	153.55	157.32	156.65	156.23	156.27
LP(3) Cl2	BD*(1) N2–H22	66.19	47.49	42.30	40.54	40.30
LP(1) Cl3	LP*(7) Cu1	72.72	64.10	63.26	63.01	63.01
LP(4) Cl3	LP*(6) Cu1	123.85	105.31	102.84	102.00	101.96
LP(4) Cl3	LP*(7) Cu1	206.65	192.67	191.04	190.50	190.50
LP(1) O1	LP*(9) Cu1	31.59	34.64	35.15	35.40	35.40
LP(1) O2	LP*(9) Cu1	36.36	37.24	37.24	37.20	37.20
LP(1) N1	LP*(6) Cu1	63.39	69.83	70.63	70.88	70.88
LP(1) N1	LP*(8) Cu1	64.52	71.55	72.72	73.18	73.22

^a LP = lone pairs, LP* = antibonding molecular orbitals of Cu. BD* = antibonding orbitals.

As the interaction between $(\text{HNEt}_3)^+$ and $[\text{Cu}(\text{pydicR}_2)\text{Cl}_3]^-$ as the electron acceptor and electron donor increases, the calculated $E^{(2)}$ value become larger, as expected. Furthermore, the increase in donating tendency from electron donors to electron acceptors is consistent with the enhancement of conjugation of the whole system from R = Me to R = Ph. The results suggest strong orbital interactions between the antibonding molecular orbitals of the Cu atom (LP*) and the antibonding orbitals of the N2–H22 bond (BD*) in the gas phase, which leads to a stabilization of 18.91 kJ/mol for $(\text{HNEt}_3)[\text{Cu}(\text{pydicMe}_2)\text{Cl}_3]$ and 21.30 kJ/mol for $(\text{HNEt}_3)[\text{Cu}(\text{pydicPh}_2)\text{Cl}_3]$, respectively. In solution with an effect of the solvents, this donor-acceptor behavior between $(\text{HNEt}_3)^+$ and $[\text{Cu}(\text{pydicMe}_2)\text{Cl}_3]^-$ leads to a reduction of the intermolecular charge transfer with lower values of $E^{(2)}$ (1.66). The table also reveals that the $E^{(2)}$ in the LP*(8) Cu1 and the BD*(1) N2–H22 and also the LP(3) Cl2 and BD*(1) N2–H22 are decreasing with an increasing dielectric constant of the solvent. The NBO analysis results illustrate that, in the gas phase, LP(4) Cl2 and LP(4) Cl1 participate as donors and the LP*(7) Cu1 acts as an acceptor with the strongest intramolecular charge transfer interactions (Table 2). In solvent environments, the $E^{(2)}$ in the LP(4) Cl2 and LP*(7) Cu1 and also the $E^{(2)}$ in the LP(4) Cl1 and LP*(7) Cu1 are enlarged with increasing dielectric constants of the solvent. However, this trend for the $E^{(2)}$ in the LP(4) Cl3 and LP*(7) Cu1 are completely reversed. The trend of charge transfer from LP(1) O1, LP(1) O2, and LP(1) N1 as donors and LP* Cu1 as an acceptor are increased with a growing dielectric constant of the solvents.

2.3. Molecular Dynamics (MD) Simulations of Bulk Solutions

In addition, we also performed molecular dynamic simulations using the GROMACS 4.5.5 package and utilizing the GROMOS force field 53A6. Six ion pairs solvated in 1200 solvent molecules were simulated for each compound. As an example, Figure 6A shows the snapshot of the $(\text{HNEt}_3)^+ \cdots [\text{Cu}(\text{pydicMe}_2)\text{Cl}_3]^-$ ion pairs solvated in MeCN after 10 ns of simulation. The anion-cation correlation lifetime in various solvents is depicted in Figure 6B. The lifetime of the hydrogen bond between the Cl2 atom of the anion and H22 of the cation for the $(\text{HNEt}_3)^+ \cdots [\text{Cu}(\text{pydicMe}_2)\text{Cl}_3]^-$ system tends to diminish along the series acetone > DMF > CH_2Cl_2 > MeCN, which is not along the general polarity (permittivity) of these solvents. The radial distribution functions ($g(r)$) between the Cl2 atom of the anion and H22 of the cation are calculated and illustrated in Figure 6C for $(\text{HNEt}_3)^+ \cdots [\text{Cu}(\text{pydicMe}_2)\text{Cl}_3]^-$ ion pairs in various solvents.

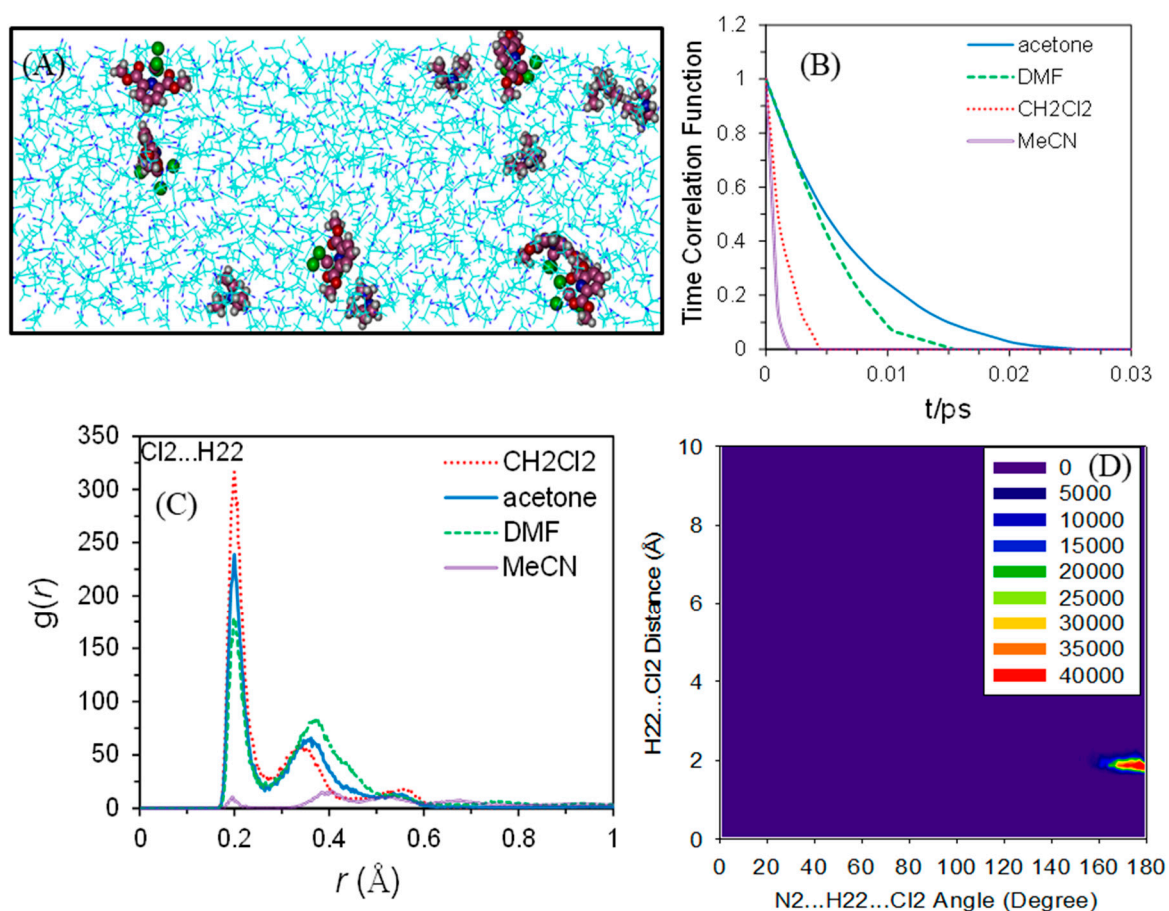


Figure 6. (A) Snapshots of the DFT calculated dynamic behavior of six ion pairs $(\text{HNEt}_3)[\text{Cu}(\text{pydicMe}_2)\text{Cl}_3]$ in MeCN. (B) Time correlation functions, (C) the radial distribution function, and (D) the combined radial/angular distribution function between the Cl2 atom of the anion and H22 of the cation in $(\text{HNEt}_3)^+ \cdots [\text{Cu}(\text{pydicMe}_2)\text{Cl}_3]^-$.

The first peak of the radial distribution function is located at around 1.84 Å, which is an indicator of a strong hydrogen bond. Combined radial/angular distribution function (CDF) is a powerful tool for defining hydrogen bond criteria, since it offers much more information than $g(r)$ [45]. The combined radial/angular distribution function (see Figure 6D) indicates that this preferred interaction occurs for N2...H22...Cl2 angles (α) between 160° and 180°.

All of these calculated data points show a marked difference between the gas phase and solvent surrounding these ion pairs and emphasizing the importance of the proper inclusion of solvents in any DFT calculations. According to our calculations, the electronic structure of the studied solutes is

influenced in a different manner by the non-coordinating CH_2Cl_2 , the weakly coordinating acetone, and MeCN and DMF, which are considered suitable ligands for Cu^{II} . With increasing polarity along the series gas phase $< \text{CH}_2\text{Cl}_2 < \text{acetone} < \text{MeCN} < \text{DMF}$ solutions, the $\text{Cl}_3\text{-Cu}$ bond is markedly elongated, the distance between the cations and anions are increased, and the dipole moments as well as the extent of charge localization of the cation and anion increases. However, the differences between CH_2Cl_2 and MeCN or DMF solutions are not very pronounced. Although more detailed kinetic calculations would be necessary to make a statement on the dissociation of the complexes in MeCN or DMF solution, we assume from the present calculations that the complexes remain stable in solution, which is important in view of the following spectroscopy and electrochemical measurements in the solution.

2.4. EPR Spectroscopy of Solids and Solutions

The X-band EPR spectrum of $[\{\text{Cu}(\text{pydic}(\text{IPh})_2)\text{Cl}\}_2(\mu\text{-Cl})_2]$ in the solid shows a very intense signal for the forbidden $\Delta M_S = \pm 2$ transition and a rhombic $\Delta M_S = \pm 1$ signal (Figure 7), which is completely in line with the binuclear character of the complex and a triplet ground state. In acetone solution, the spectrum is essentially retained and, thus, the binuclear character remains unchanged. A similar spectrum with very similar g values has been reported for $[\{\text{Cu}(\text{pydicEt}_2)\text{Cl}\}_2(\mu\text{-Cl})_2]$ [23], while the derivative $[\{\text{Cu}(\text{pydic}^i\text{Pr}_2)\text{Cl}\}_2(\mu\text{-Cl})_2]$ exhibits a markedly different averaged g value (Table 3) and no $\Delta M_S = \pm 2$ transition is observed. The difference has been attributed to the different geometries for the central $\text{Cu}(\mu\text{-Cl})_2\text{Cu}$ unit, which is planar for the pydicEt_2 complex but bent for the *iso*-propyl derivative [23]. Thus, our results are fully in line with the DFT-calculated structure of $[\{\text{Cu}(\text{pydic}(\text{IPh})_2)\text{Cl}\}_2(\mu\text{-Cl})_2]$, which shows a planar $\text{Cu}(\mu\text{-Cl})_2\text{Cu}$ core (Figure 1). Although the averaged g value is quite similar for the related binuclear Cu^{II} complex $[\{\text{Cu}(\text{pydotH}_2)\text{Cl}\}_2(\mu\text{-Cl})_2]$ ($\text{pydotH}_2 = 2,6\text{-bis}(1\text{-hydroxy-1-}o\text{-tolyl-ethyl-}\eta^2\text{-O,O'})\text{pyridine}$) [46], the g anisotropy Δg is markedly increased, while the $\Delta M_S = \pm 2$ is far less intense. This reflects the different “ligand setting” in this complex containing an ONO pincer ligand based on pyridine-2,6-dimethanol. As deduced from EXAFS data, the O, N, O atoms of the pydotH_2 ligand and the bridging chlorido ligand form a square plane of the tightly bound ligands. From this bridging Cl^- , an elongated Cu-Cl bond connects to the second Cu^{II} , while the terminal chloride ligand has a short Cu-Cl bond [46]. Thus, while in the binuclear complexes $[\{\text{Cu}(\text{pydicR}_2)\text{Cl}\}_2(\mu\text{-Cl})_2]$ with $\text{R} = \text{Me}, \text{Et}, ^i\text{Pr}$ and IPh , the tight binding ligands are N, Cl, and $2 \times \mu\text{-Cl}$ with the two square planes fused by the bridging $\mu\text{-Cl}$ atoms. In the pydotH_2 complex, the two square planes O,N,O, $\mu\text{-Cl}$ and the central $\text{Cu}(\mu\text{-Cl})_2\text{Cu}$ core are perpendicular to each other. The EPR spectra fully reflect this difference.

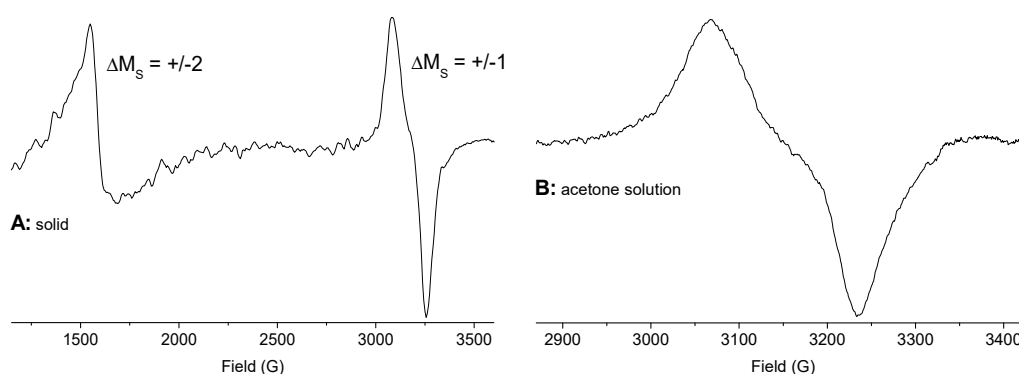


Figure 7. X-band EPR spectra of $[\{\text{Cu}(\text{pydic}(\text{IPh})_2)\text{Cl}\}_2(\mu\text{-Cl})_2]$ at 298 K. (A) in the solid. (B) in acetone solution.

The mononuclear compounds $(\text{HNEt}_3)[\text{Cu}(\text{pydicMe}_2)\text{Cl}_3]$ and $(\text{HNEt}_3)[\text{Cu}(\text{pydicPh}_2)\text{Cl}_3]$ reveal EPR spectra of axial symmetry with $g_{\parallel} > g_{\perp}$ in the solid (Figure 8), which is typical for elongated octahedral or square pyramidal Cu^{II} complexes [23,47–52]. The Cu hyperfine structure (coupling

to the ^{63}Cu (69.17%) and ^{65}Cu (30.83%) nuclei with $I = 3/2$ [53]) was not observed in line with observations for similar mononuclear complexes [46,52]. A rhombic EPR spectrum was reported for the complex $[\text{Cu}(\text{pydotH}_2)(\text{DMF})\text{Cl}_2]$ [46], which has an axially elongated distorted pseudo-octahedral geometry with the O,N,O ligand located in the square plane of tight Cu–ligand bonds. Yet, in $(\text{HNEt}_3)[\text{Cu}(\text{pydicMe}_2)\text{Cl}_3]$ and $(\text{HNEt}_3)[\text{Cu}(\text{pydicPh}_2)\text{Cl}_3]$, the N, Cl_3 coordination represents the short = strong bonds and the $\text{O}_{\text{carbonyl}}$ functions are in the elongated positions. Nevertheless, the averaged g values and g anisotropy (Δg) are very similar. Far smaller averaged g values were reported for the square pyramid or trigonal bipyramidal complexes listed in Table 3. Thus, the observed spectra represent the overall geometry around Cu^{II} than the ligand strength of Cl^- , DMF, and O atoms in the O, N, O ligands.

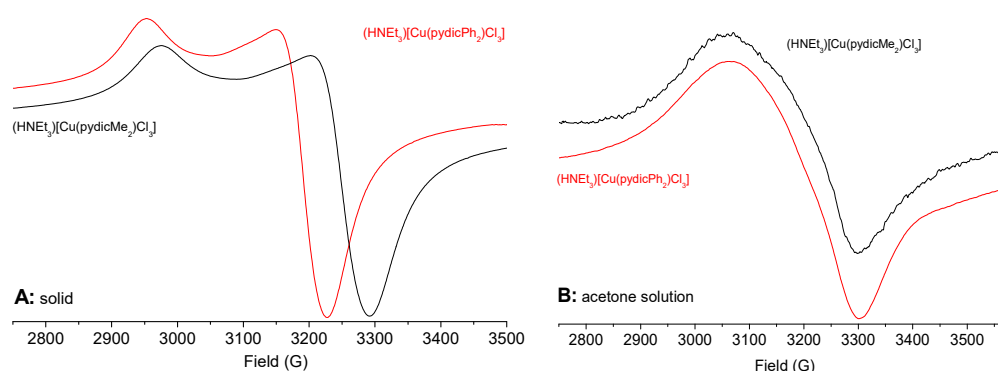


Figure 8. X-band EPR spectra of $(\text{HNEt}_3)[\text{Cu}(\text{pydicMe}_2)\text{Cl}_3]$ and $(\text{HNEt}_3)[\text{Cu}(\text{pydicPh}_2)\text{Cl}_3]$. (A) in the solid, (B) in acetone solution measured at 298 K.

Table 3. X-band EPR data of the reported and comparable Cu^{II} complexes ^a.

Compounds	g_{av}	g_{\parallel} or g_1	g_{\perp} or g_2	g_3	Δg	State
reported compounds						
$[\{\text{Cu}(\text{pydic}(\text{IPh})_2)\text{Cl}_2(\mu\text{-Cl})_2]$	2.157	2.260	2.115	2.095	0.165	solid
$[\{\text{Cu}(\text{pydic}(\text{IPh})_2)\text{Cl}_2(\mu\text{-Cl})_2]$	2.130	2.197	2.102	2.091	0.106	acetone
$(\text{HNEt}_3)[\text{Cu}(\text{pydicMe}_2)\text{Cl}_3]$	2.182	2.351	2.098		0.253	solid
$(\text{HNEt}_3)[\text{Cu}(\text{pydicMe}_2)\text{Cl}_3]$	2.131	2.211	2.091		0.120	acetone
$(\text{HNEt}_3)[\text{Cu}(\text{pydicPh}_2)\text{Cl}_3]$	2.196	2.362	2.113		0.249	solid
$(\text{HNEt}_3)[\text{Cu}(\text{pydicPh}_2)\text{Cl}_3]$	2.126	2.201	2.089		0.112	acetone
related mononuclear complexes						
$[\text{Cu}(\text{pydic})(\text{H}_2\text{O})_2]$ (sqp) ^b	2.156	2.324	2.102	2.043	0.281	solid
$[\text{Cu}(\text{pydimH}_2)\text{Cl}_2]$ (sqp) ^c	2.158	2.311	2.094	2.068	0.243	solid
$[\text{Cu}(\text{pydipH}_2)\text{Cl}_2]$ (tbp) ^c	2.138	2.220	2.220	1.973 ^e	0.223	solid
$[\text{Cu}(\text{pydotH}_2)(\text{DMF})\text{Cl}_2]$ (aeo) ^c	2.194	2.353	2.120	2.108	0.245	solid
related binuclear complexes						
$[\{\text{Cu}(\text{pydicEt}_2)\text{Cl}_2(\mu\text{-Cl})_2]$ ^d	2.147	2.21	2.12	2.11	0.100	solid
$[\{\text{Cu}(\text{pydic}^i\text{Pr}_2)\text{Cl}_2(\mu\text{-Cl})_2]$ ^d	2.130	2.17	2.16	2.06	0.110	solid
$[\{\text{Cu}(\text{pydotH}_2)\text{Cl}_2(\mu\text{-Cl})_2]$ ^c	2.148	2.418	2.081	1.946	0.472	solid

^a measured at 298 K; g_{av} = averaged g value = $(g_{\parallel} + 2g_{\perp})/3$ or $(g_1 + g_2 + g_3)/3$; $\Delta g = g_{\parallel} - g_{\perp}$ or $g_1 - g_3$. ^b From Reference [52]. ^c From Reference [46]. sqp = square pyramidal, tbp = trigonal bipyramidal, aeo = axially elongated pseudo-octahedral. ^d From Reference [23].

Samples dissolved in acetone or MeCN (at ambient temperatures) exhibit axial signal symmetry even though the averaged g values and the g anisotropy (Δg) are markedly decreased. We conclude that the ion pairs and the anionic complexes in $(\text{HNEt}_3)[\text{Cu}(\text{pydicR}_2)\text{Cl}_3]$ are basically retained in acetone or MeCN solution with minor alterations in complex geometry. This is completely in line with our DFT calculations showing changes in the geometry and charge transfer of the ion pairs upon solvation and likely shows no dissociation.

2.5. UV–Vis Absorption Spectroscopy

The binuclear complex $[\{\text{Cu}(\text{pydic}(\text{IPh})_2)\text{Cl}\}_2(\mu\text{-Cl})_2]$ and the mononuclear compounds $(\text{HNEt}_3)[\text{Cu}(\text{pydicMe}_2)\text{Cl}_3]$ and $(\text{HNEt}_3)[\text{Cu}(\text{pydicPh}_2)\text{Cl}_3]$ dissolved in MeCN show intense UV bands around 290 or 260, respectively, which is assignable to ligand-centered $\pi\text{-}\pi^*$ transitions (Table 4, spectra in the Supplementary Materials). The three complexes all show a characteristic absorption band at around 460 nm, which is assignable to a ligand(Cl)-to-metal(Cu) charge transfer LMCT transition. In the visible range, broad bands assigned to d–d transitions ($a_2, b_1, b_2 \rightarrow a_1$ in C_{2v} symmetry) were observed. Their exact energies are difficult to determine but lie around 820 nm for $(\text{HNEt}_3)[\text{Cu}(\text{pydicMe}_2)\text{Cl}_3]$, 890 nm for $(\text{HNEt}_3)[\text{Cu}(\text{pydicPh}_2)\text{Cl}_3]$, and 830 nm for $[\{\text{Cu}(\text{pydic}(\text{IPh})_2)\text{Cl}\}_2(\mu\text{-Cl})_2]$. These are in line with values recently reported for related Cu^{II} complexes with O,N,O ligands of the pyridine-2,6-dimethanol type [46,54]. In the spectrum of $\text{K}_2[\text{CuCl}_4]$ in MeCN, the long wavelength d-d band is observed at 1074 nm, which is in line with a markedly stronger ligand field for the $[\text{Cu}(\text{pydicR}_2)\text{Cl}_3]^-$ and $[\{\text{Cu}(\text{pydic}(\text{IPh})_2)\text{Cl}\}_2(\mu\text{-Cl})_2]$ complexes.

Table 4. Absorption maxima for Cu^{II} complexes ^a.

Compounds	λ/nm ($\epsilon/\text{L}\cdot\text{mol}^{-1}\cdot\text{cm}^{-1}$) ^c
$(\text{HNEt}_3)[\text{Cu}(\text{pydicMe}_2)\text{Cl}_3]$	261 (48400), 462 (3290), 822 (160)
$(\text{HNEt}_3)[\text{Cu}(\text{pydicPh}_2)\text{Cl}_3]$	261 (44400), 307 (14400) ^b , 462 (4580), 890 (310)
$[\{\text{Cu}(\text{pydic}(\text{IPh})_2)\text{Cl}\}_2(\mu\text{-Cl})_2]$	289 (27100), 464 (3740), 830 (200)
$\text{K}_2[\text{CuCl}_4]$	312, 346sh, 462, 1074

^a Measured in MeCN. ^b Absorption assigned to $\pi(\text{Ph})\text{-}\pi(\text{Py})$ transitions. ^c extinction coefficient.

2.6. Electrochemical Measurements

The electrochemical properties of the new complexes and the new ligand $\text{pydic}(\text{IPh})_2$ were studied by cyclic voltammetry in $\text{MeCN}/^m\text{Bu}_4\text{NPF}_6$ solution. The complex $[\{\text{Cu}(\text{pydic}(\text{IPh})_2)\text{Cl}\}_2(\mu\text{-Cl})_2]$ shows a reversible redox wave around 0 V vs. ferrocene/ferrocenium, which can be assigned to the $\text{Cu}^{\text{II}}/\text{Cu}^{\text{I}}$ couple (Figure 9). Additionally, an irreversible oxidation wave at 0.73 V and an irreversible reduction wave at -1.33 V were observed. They both occurred for the uncoordinated ligand at similar potentials (Table 5) and were, thus, assigned to ligand-centered processes. Assuming two electrons for the reversible $\text{Cu}^{\text{II}}/\text{Cu}^{\text{I}}$ wave of the binuclear complex, the oxidation wave is markedly larger and more than two electrons might be involved in this process. The redox features of the mononuclear compounds $(\text{HNEt}_3)[\text{Cu}(\text{pydicMe}_2)\text{Cl}_3]$ and $(\text{HNEt}_3)[\text{Cu}(\text{pydicPh}_2)\text{Cl}_3]$ are very similar, with a reversible $\text{Cu}^{\text{II}}/\text{Cu}^{\text{I}}$ wave at around 0.1 V, irreversible oxidations at around 1 V, and reductions at around -1.3 V (Figure S4 in the Supplementary Materials). For the phenyl derivative $[\text{Cu}(\text{pydicPh}_2)\text{Cl}_3]^-$, the second reduction wave is partially reversible, while the methyl derivative shows a broad irreversible wave. The bulky phenyl groups seem to stabilize the reduced complex, which is in line with the idea that the reduction is ligand-centered.

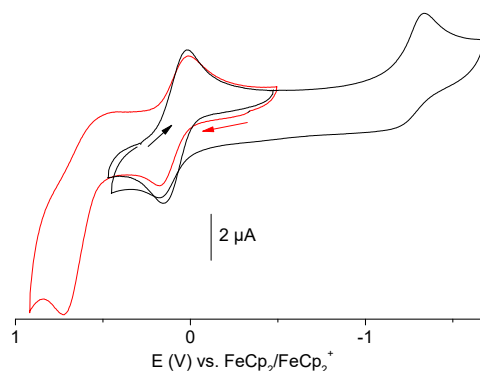


Figure 9. Cyclic voltammograms of $[\{\text{Cu}(\text{pydic}(\text{IPh})_2)\text{Cl}\}_2(\mu\text{-Cl})_2]$ in $\text{MeCN}/^m\text{Bu}_4\text{NPF}_6$.

Table 5. Selected electrochemical data ^a.

Compounds	E_{pa} ox	$E_{\frac{1}{2}}$ Cu ^I /Cu ^{II}	E_{pc} red
pydic(IPh) ₂	0.72	-	-1.52
pydicPh ₂	0.91	-	-1.63
pydicMe ₂	0.86	-	-1.60
[[Cu(pydic(IPh) ₂)Cl] ₂ (μ-Cl) ₂]	0.73	0.08	-1.33
(HNEt ₃)[Cu(pydicPh ₂)Cl ₃]	1.11	0.09	-1.32
(HNEt ₃)[Cu(pydicMe ₂)Cl ₃]	0.84	0.14	-1.33
K ₂ [CuCl ₄]	1.12	0.08	-1.48

^a From cyclic voltammetry in MeCN/ⁿBu₄NPF₆ solutions. Half-wave potentials $E_{\frac{1}{2}}$ for reversible waves, cathodic peak potentials E_{pc} for irreversible reduction, and anodic peak potentials E_{pa} for irreversible oxidation. All potentials in V vs. FeCp₂/FeCp₂⁺.

Spectro-electrochemical (SEC), in situ UV–vis absorption spectra during cathodic or anodic electrolysis measurements of (HNEt₃)[Cu(pydicPh₂)Cl₃] and [[Cu(pydic(IPh)₂)Cl]₂(μ-Cl)₂] confirm the full reversibility of the Cu^{II}/Cu^I waves. However, no conclusive spectra were obtained for the reduced species at around -1.3 or the oxidized complexes at around +1 V (for figures, see Supplementary Materials). Importantly, the reduction wave at -1.3 V for (HNEt₃)[Cu(pydicPh₂)Cl₃], which appears reversible in the relatively fast cyclic voltammetry experiment with a timescale of a few seconds turns out to be completely irreversible in the much slower SEC experiments, which are run on a minute timescale.

3. Experimental Section

3.1. Methods and Instrumentation

NMR spectra were recorded on a Bruker Avance II 300 MHz spectrometer (Bruker, Rheinhausen, Germany), using a triple resonance ¹H, ⁿBB inverse probe head. The unambiguous assignment of the ¹H and ¹³C resonances was obtained from ¹H NOESY, ¹H COSY, gradient selected ¹H, ¹³C HSQC, and HMBC experiments. All 2D NMR experiments were performed using standard pulse sequences from the Bruker pulse program library. Chemical shifts were relative to TMS. UV–vis absorption spectra were measured on a Shimadzu UV-3600 photo spectrometer (Shimadzu Europe, Duisburg, Germany). Elemental analyses were carried out using a HEKATECH CHNS EuroEA 3000 Analyzer (Hekatech, Wegberg, Germany). EPR spectra were recorded in the X-band on a Bruker System ELEXSYS 500E equipped with a Bruker Variable Temperature Unit ER 4131VT (500 to 100 K) (Bruker, Rheinhausen, Germany). The *g* values were calibrated using a DPPH sample. Electrochemical experiments were carried out in 0.1 M ⁿBu₄NPF₆ solutions using a three-electrode configuration (glassy carbon working electrode, Pt counter electrode, Ag/AgCl pseudo reference), an Autolab PGSTAT30 potentiostat (Metrohm, Filderstadt, Germany), and a function generator. Experiments were run at a scan rate of 100 mV/s at ambient temperature. The ferrocene/ferrocenium couple (FeCp₂/FeCp₂⁺) served as the internal reference. UV–vis spectro-electrochemical measurements were performed with an optical transparent thin-layer electrochemical (OTTLE) cell [55,56].

3.2. Crystal Structure Determination

The measurements were performed at 293(2) K using graphite mono-chromatized Mo K α radiation ($\lambda = 0.71073$ Å) on IPDS II (STOE and Cie., Darmstadt, Germany). The structures were solved by direct methods using SHELX-97 and WinGX (SHELXS-97) [57–59] and refined by full-matrix least-squares techniques against F^2 (SHELXL-2017/1) [60,61]. The numerical absorption corrections (X-RED V1.22; Stoe & Cie, 2001) were performed after optimizing the crystal shapes using the X-SHAPE V1.06 (Stoe & Cie, 1999) [62,63]. The non-hydrogen atoms were refined with anisotropic displacement parameters. H atoms were included by using appropriate riding models. CCDC 1878796 ([Cu(OH₂)₆][[Cu(pydic)₂(μ-Cl)₂]], 1878795 ((HNEt₃)[Cu(pydicMe₂)Cl₃]), and 1878792 (pydic(IPh)₂)

contain the full crystallographic data. These data can be obtained free of charge at www.ccdc.cam.ac.uk/conts/retrieving.html or from the Cambridge Crystallographic Data Center, 12 Union Road, Cambridge, CB2 1EZ UK. Fax: +44-1223-336-033; Email: deposit@ccdc.cam.ac.uk.

3.3. Quantumchemical and Molecular Dynamics Calculations

DFT-calculations on the structures of mononuclear [Cu(pydic(IPh)₂)Cl₂] vs. binuclear [{Cu(pydic(IPh)₂)Cl₂(μ-Cl)₂] were carried out on a def-SV(P)[64]/B3LYP [65–67] level using the TURBOMOLE [68] program package and TmoleX user interface [69].

(HNEt₃)[Cu(pydicR₂)Cl₃] (R = Me or Ph) structures were optimized using DFT calculations at the B3LYP/6–31+G(d,p) level in different environments (gas phase, various solvents) using the Gaussian 09 program [70]. The Cu atom was treated using LANL2DZ relativistic pseudo potentials. The solvent effect was introduced by applying the polarized continuum model (PCM) embedded in the Gaussian 09 package. In the natural bond, the orbital (NBO) analysis and the donor and acceptor interaction energies can be estimated through the second-order perturbation theory, described using the equation below.

$$E^{(2)} = q_i \frac{F(i, j)^2}{\varepsilon_i - \varepsilon_j}$$

where q_i is the donor orbital occupancy, ε_j and ε_i are diagonal elements, and $F(i, j)$ is the off-diagonal NBO Fock matrix element.

Molecular dynamics (MD) simulations on (HNEt₃)[Cu(pydicR₂)Cl₃] (R = Me or Ph) were carried out using the GROMACS package [71] and utilizing the GROMOS force field 53A6 [72]. Six-ion pairs solvated in 1200 solvent molecules were simulated for each compound. The equations of motion have been solved by the leapfrog integrator with a time step of 2 fs. After initial energy minimizations and preliminary simulations adjustments in NVT and NPT ensembles, MD simulations were extended for an additional time of 10 ns collecting statistical data under the NPT condition at $T = 298$ K with periodic boundary conditions in all directions. The temperature was maintained at 298 K using the Berendsen thermostat [73] and the pressure was kept at 1 bar by coupling semi-isotropically to a barostat with a coupling constant of 1 ps. Both the electrostatic and van der Waals interactions used a short-range cutoff of 1.2 nm and the long-range electrostatics were evaluated using the particle mesh Ewald (PME) method [74].

3.4. Syntheses

3.4.1. General

Water-free reactions were carried out under inert gas conditions and performed using Schlenk techniques. Solvents were dried using a MBRAUN MB SPS-800 solvent purification system. Pyridine-2,6-dicarbonyl dichloride [51] was synthesized according to a literature procedure.

Data *pyridine-2,6-dicarbonyl dichloride*: Elemental analysis calcd. for C₇H₃NO₂Cl₂ (204.01): C 41.21, H 1.48, N 6.87; found: C 41.13, H 1.30, N 6.83%. ¹H NMR (300 MHz, acetone-d₆): $\delta = 8.55$ – 8.41 (m, 3H, 3,4,5Py). ¹³C NMR (75.47 MHz, acetone-d₆): $\delta = 170$ (2C, C=O), 150 (2C, 2,6Py), 142 (1C, 4Py), 131 (2C, 3,5Py) ppm.

3.4.2. Synthesis of bis(2-iodophenyl)pyridine-2,6-dicarboxylic ester pydic(IPh)₂ and [Cu(pydic(IPh)₂)Cl₂(μ-Cl)₂]

Synthesis of pydic(IPh)₂. A total of 1.0 g (5 mmol) pyridine-2,6-dicarbonyl dichloride was dissolved in 20 mL dry diethyl ether. In addition, 2.3 g (10 mmol) of 2-iodo-phenol were dissolved in 30 mL dry diethyl ether. Furthermore, 10 mg 4-dimethylaminopyridine (5%_{mol}) and 0.7 mL NEt₃ were added to the alcohol mixture, which was then cooled using an ice bath. The acid chloride solution was dropped slowly into the alcohol mixture and precipitation of the product started immediately. After stirring for 1 h at 0 °C, 0.7 mL NEt₃ were added at an ambient temperature and the mixture was stirred for 16 h.

The formed colorless precipitate was filtered off and washed with 5 mL diethyl ether. The remaining powder was dried yielding 2.35 g (82%) of a colorless solid. Elemental analysis calcd. for $C_{19}H_{11}NO_4I_2$ (571.10): C 39.96, H 1.94, N 2.45; found: C 39.89, H 1.93, N 2.43%. 1H NMR (300 MHz, $dmf-d_7$): δ = 8.64 (d, 2H, 3,4Py), 8.47 (t, 1H, 5Py), 7.94 (d, 2H, 3Ph), 7.51 (t, 2H, 5Ph), 7.47 (d, 2H, 6Ph), 7.11 (t, 2H, 4Ph) ppm.

Synthesis of $[Cu(pydic(IPh)_2)Cl]_2(\mu-Cl)_2$. 100 mg (0.18 mmol) pydic(IPh)₂ were dissolved in 15 mL MeOH. 24 mg (0.18 mmol) anhydrous CuCl₂ were dissolved in 10 mL MeOH and both solutions were mixed and stirred at an ambient temperature for 16 h. The solvent was evaporated to yield a brown powder. Recrystallization from MeOH gave 85 mg (67%) of brown microcrystalline material. Elemental analysis calcd. for $C_{19}H_{11}CuCl_2NO_4I_2$ (705.56): C 32.34, H 1.57, N 1.99; found: C 32.33, H 1.62, N 2.02.

3.4.3. One Pot Reactions

Synthesis of $(HNEt_3)[Cu(pydicMe_2)Cl_3]$. 100 mg (0.5 mmol) pyridine-2,6-dicarbonyl dichloride were dissolved in 15 mL dried MeOH while 67 mg (0.5 mmol) anhydrous CuCl₂ were added, which was followed by 1 mL (excess) anhydrous NEt₃. The reaction mixture was stirred at ambient temperature for 16 h. The resulting green solution was evaporated to dryness and the residue was recrystallized from MeOH solution to yield 175 mg (0.37 mmol, 75%) green-brown crystals. $C_{15}H_{25}CuCl_3N_2O_4$ (467.27) calcd.: C 38.56, H 5.39, N 6.00; found: C 38.63, H 5.39, N 6.02%.

Synthesis of $(HNEt_3)[Cu(pydicPh_2)Cl_3]$. A total of 200 mg (1 mmol) pyridine-2,6-dicarbonyl dichloride were mixed with 15 g phenol and 132 mg (1 mmol) anhydrous CuCl₂ followed by the addition of 1 mL NEt₃. The mixture was warmed up to 50 °C to get a clear homogenous mixture (melting point of phenol = 40.5 °C) and stirred for 96 h. During that time, the excess phenol solidified in the upper part of the flask and the product complex remained as brown oil. The oil was transferred to a new flask and cooled down to 20 °C, upon which the oil solidified as a brownish powder. The crude product was suspended in acetone and carefully filtered. Slow evaporation yielded 350 mg (0.6 mmol, 60%) of a green-yellow microcrystalline powder. $C_{25}H_{29}CuCl_3N_2O_4$ (591.41) calcd.: C 50.77, H 4.94, N 4.74; found: C 50.72, H 4.98, N 4.76%.

3.4.4. Complexes from pydicCl₂ Hydrolysis

In a typical reaction, 100 mg (0.5 mmol) pyridine-2,6-dicarbonyl dichloride were dissolved in 15 mL moist MeOH. 85 mg (0.5 mmol) CuCl₂·2H₂O and 1 mL (excess) NEt₃ were added and the whole mixture was stirred at an ambient temperature for 16–24 h. The resulting green solutions were slowly evaporated and individual crystals were collected. Thus, 33 mg (24%) turquoise crystals of $[Cu(pydic)(OH_2)_2]_n$ were obtained. Elemental analysis calcd. for $C_7H_7CuNO_6$ (264.68): C 31.76, H 2.67, N 5.29; found: C 31.79, H 2.72, N 5.24%, see also the XRD Section. In the same way, 21 mg (12%) blue-green crystals of $[Cu(OH_2)_6][Cu(pydic)_2(\mu-Cl)_2]$ were obtained. Elemental analysis calcd. for $C_{14}H_{18}Cu_3Cl_2N_2O_{14}$ (699.84): C 21.74, H 1.82, N 3.62; found: C 21.80, H 1.79, N 3.58%, see also XRD section.

4. Conclusions

New Cu^{II} complexes of the pyridine-2,6-dicarboxylic ester ligands (pydicR₂; with R = Me, Ph and IPh) were synthesized and characterized. The pyridine-2,6-carboxylic esters pydicR₂ with R = Me or Ph form the unprecedented mononuclear Cu^{II} complexes $[Cu(pydicR_2)Cl_3]^-$ in one-pot reactions starting from pyridine-2,6-carboxylchloride pydicCl₂, anhydrous Cu^{II} chloride, and NEt₃ in MeOH or PhOH solution under non-aqueous conditions. The triethyl ammonium salts $(HNEt_3)[Cu(pydicR_2)Cl_3]$ were isolated. The methyl derivative was crystallized to allow an XRD structure determination. Synthesis attempts in the presence of water yielded the Cu^{II} complexes $[Cu(pydic)(OH_2)_2]_n$ and $[Cu(OH_2)_6][Cu(pydic)_2(\mu-Cl)_2]$ resulting from pydicCl₂ hydrolysis. The new pydic(IPh)₂ (IPh = 2-iodo-phenyl) ester ligand was synthesized and reacted with anhydrous CuCl₂ yielding the

new binuclear complex $[\text{Cu}(\text{pydic}(\text{IPh})_2\text{Cl})_2(\mu\text{-Cl})_2]$. EPR, UV-vis absorption spectroscopic and electrochemical investigations confirm similarities between copper complexes of pydic ester ligands and corresponding Cu complexes of pyridine-2,6-dialcohols. HOMO-LUMO gap, dipole moments, and electrostatic potential maps for the ion pairs $(\text{HNEt}_3)[\text{Cu}(\text{pydicR}_2)\text{Cl}_3]$ are calculated using DFT methods. These quantities were decreasing along the series $\text{DMF} > \text{MeCN} > \text{acetone} > \text{CH}_2\text{Cl}_2 \gg \text{gas phase}$. The second order delocalization energies obtained from the NBO analysis confirm the occurrence of the intramolecular charge transfer between the $(\text{HNEt}_3)^+$ and $[\text{Cu}(\text{pydicR}_2)\text{Cl}_3]^-$ ions. However, increasing the dielectric constant of the solvent environment leads to a reduction of charge transfers between cations and anions. Furthermore, time correlation functions as well as radial and combined distribution functions between cations and anions were calculated by MD simulations. All of these data show a marked difference between the gas phase and a different solvent media ranging from the non-coordinating CH_2Cl_2 and the weakly coordinating acetone to the MeCN and DMF, which are both frequently used as ligands in Cu^{II} complexes. We assume that the spectroscopy and electrochemistry in such solutions represent the complexes under study and not dissociated Cu^{II} species.

Supplementary Materials: The following are available online at <http://www.mdpi.com/2304-6740/7/4/53/s1>. (A) Figures S1–S10 showing crystal and molecular structures, CVs, UV-vis absorption spectra and electrostatic potential maps of $(\text{HNEt}_3)[\text{Cu}(\text{pydicR}_2)\text{Cl}_3]$ in solvents. (B) Tables S1–S8 presenting full crystal structure and refinement data alongside with calculated structure parameters and second-order perturbation energies. (C) Experimental details on structure solution and description of structural details of $\text{pydic}(\text{IPh})_2$ and $[\text{Cu}(\text{OH}_2)_6][[\text{Cu}(\text{pydic})_2(\mu\text{-Cl})_2]$. (D) Cif and Checkcif files of the ligand $\text{pydic}(\text{IPh})_2$ and the compounds $[\text{Cu}(\text{OH}_2)_6][[\text{Cu}(\text{pydic})_2(\mu\text{-Cl})_2]$ and $(\text{HNEt}_3)[\text{Cu}(\text{pydicMe}_2)\text{Cl}_3]$.

Author Contributions: K.B. carried out synthesis, analysis, and spectroscopic and electrochemical analysis of the compounds. K.B. and A.S. collected data and solved and refined XRD datasets. A.S., M.H.D., and A.R.Z. performed the quantum chemical calculations. A.R.Z. coordinated these calculations. A.K. designed the project and wrote the manuscript. All authors have given approval to the final version of the manuscript.

Funding: This research was funded by Studienstiftung des Deutschen Volkes (K.B.). A.K. acknowledges the German Academic Exchange Service (DAAD)—KD_0001052598-2 for a short-time guest lectureship and the Shiraz University.

Acknowledgments: We thank Ingo Pantenburg (University of Cologne) for crystal data collection.

Conflicts of Interest: The authors declare no conflict of interest.

References

1. Xiang, S.; Bao, D.-X.; Wang, J.; Li, Y.-C.; Zhao, X.-Q. Luminescent lanthanide coordination compounds with pyridine-2,6-dicarboxylic acid. *J. Lumin.* **2017**, *186*, 273–282. [[CrossRef](#)]
2. Celestine, M.J.; Bullock, J.L.; Boodram, S.; Rambaran, V.H.; Holder, A.A. Interesting properties of p-, d-, and f-block elements when coordinated with dipicolinic acid and its derivatives as ligands: Their use as inorganic pharmaceuticals. *Rev. Inorg. Chem.* **2015**, *35*, 57–67. [[CrossRef](#)]
3. Kirillov, A.M.; Shul'Pin, G.B. Pyrazinecarboxylic acid and analogs: Highly efficient co-catalysts in the metal-complex-catalyzed oxidation of organic compounds. *Coord. Chem. Rev.* **2013**, *257*, 732–754. [[CrossRef](#)]
4. Teo, P.; Hor, T.A. Spacer directed metallo-supramolecular assemblies of pyridine carboxylates. *Coord. Chem. Rev.* **2011**, *255*, 273–289. [[CrossRef](#)]
5. Abdelhameed, R.M.; Ananias, D.; Silva, A.M.S.; Rocha, J. Building Light-Emitting Metal–Organic Frameworks by Post-Synthetic Modification. *ChemistrySelect* **2017**, *2*, 136–139. [[CrossRef](#)]
6. Yang, R.; Li, H.H.; Van Hecke, K.; Cui, G.H. Cobalt(II) and Copper(II) Complexes Constructed from Bis(benzimidazole) and 2,6-Pyridinedicarboxylate Co-ligands: Synthesis, Crystal Structures, and Catalytic Properties. *Z. Anorg. Allgem. Chem.* **2015**, *641*, 642–649. [[CrossRef](#)]
7. Derikvand, Z.; Dorosti, N.; Hassanzadeh, F.; Shokrollahi, A.; Mohammadpour, Z.; Azadbakht, A. Three new supramolecular compounds of copper(II), cobalt(II) and zirconium(IV) with pyridine-2,6-dicarboxylate and 3,4-diaminopyridine: Solid and solution states studies. *Polyhedron* **2012**, *43*, 140–152. [[CrossRef](#)]

8. Kim, M.K.; Bae, K.-L.; Ok, K.M. From Pincers to Steps: Synthesis, Structure, Characterization, and Transformation of a New Helical Calcium–Organic Framework, $\text{Ca}[\text{NC}_5\text{H}_3(\text{CO}_2)_2](\text{H}_2\text{O})_{1.5}$. *Cryst. Growth Des.* **2011**, *11*, 930–932. [[CrossRef](#)]
9. Stavila, V.; Bulimestru, I.; Gulea, A.; Colson, A.C.; Whitmire, K.H. Hexaaquacobalt(II) and hexaaquanickel(II) bis(μ -pyridine-2,6-dicarboxylato)bis[(pyridine-2,6-dicarboxylato)bismuthate(III)] dihydrate. *Acta Crystallogr. Sect. C Cryst. Struct. Commun.* **2011**, *67*, m65–m68. [[CrossRef](#)]
10. Zhang, G.-C.; Chen, S.-P.; Yang, Q.; Gao, S.-L. Thermochemistry on $\text{K}_2[\text{M}(\text{DPA})_2] \cdot 7\text{H}_2\text{O}(\text{s})$ ($\text{M} = \text{Cu}$ and Ni , $\text{H}_2\text{DPA} = \text{pyridine-2,6-dicarboxylic acid}$). *Thermochim. Acta* **2011**, *518*, 66–71. [[CrossRef](#)]
11. Das, B.; Baruah, J.B. Coordinated cations in dipicolinato complexes of divalent metal ions. *Inorg. Chim. Acta* **2010**, *363*, 1479–1487. [[CrossRef](#)]
12. Felloni, M.; Blake, A.J.; Hubberstey, P.; Wilson, C.; Schröder, M. Solvent Control of Supramolecular Architectures Derived from 4,4'-Bipyridyl-Bridged Copper(II) Dipicolinate Complexes. *Cryst. Growth Des.* **2009**, *9*, 4685–4699. [[CrossRef](#)]
13. Furet, E.; Costuas, K.; Rabiller, P.; Maury, O. On the Sensitivity of f Electrons to Their Chemical Environment. *J. Am. Chem. Soc.* **2008**, *130*, 2180–2183. [[CrossRef](#)]
14. Katada, H.; Seino, H.; Mizobe, Y.; Sumaoka, J.; Komiyama, M. Crystal structure of Ce(IV)/dipicolinate complex as catalyst for DNA hydrolysis. *J. Biol. Inorg. Chem.* **2008**, *13*, 249–255. [[CrossRef](#)] [[PubMed](#)]
15. Hakimi, M.; Mardani, Z.; Moeini, K.; Mohr, F. Coordination behavior of dimethyl pyridine-2,6-dicarboxylate towards mercury(II), cadmium(II) and chromium(III) in the solid- and gaseous state supported by CSD studies. *Polyhedron* **2015**, *102*, 569–577. [[CrossRef](#)]
16. Hakimi, M.; Moeini, K.; Mardani, Z.; Schuh, E.; Mohr, F. Silver(I) coordination polymer and nine-coordinated cadmium(II) complex with dimethyl pyridine-2,6-dicarboxylate supported by solid state and electrochemical studies. *J. Coord. Chem.* **2013**, *66*, 1129–1141. [[CrossRef](#)]
17. Kapoor, P.; Pathak, A.; Kaur, P.; Venugopalan, P.; Kapoor, R. Steric control of coordination: Unusual coordination mode of dimethylpyridine-2,6-dicarboxylate in a new dinuclear copper(II) complex $[(\text{dmpc})(\text{Cl})(\mu\text{-Cl})\text{Cu}_2(\mu\text{-Cl})(\text{Cl})(\text{dmpc})]$ and reversal of the coordination mode in $[\text{Cu}(\text{dmpc})(\text{H}_2\text{O})_3](\text{ClO}_4)_2$. *Trans. Met. Chem.* **2004**, *29*, 251–258. [[CrossRef](#)]
18. Steinkamp, T.; Karst, U. Detection scheme for bioassays based on 2,6-pyridinedicarboxylic acid derivatives and enzyme-amplified lanthanide luminescence. *Anal. Chim. Acta* **2004**, *526*, 27–34. [[CrossRef](#)]
19. Pointillart, F.; Bourdolle, A.; Cauchy, T.; Maury, O.; le Gal, Y.; Golhen, S.; Cador, O.; Ouahab, L. In Solution Sensitization of Er(III) Luminescence by the 4-Tetrathiafulvalene-2,6-pyridinedicarboxylic Acid Dimethyl Antenna Ligand. *Inorg. Chem.* **2012**, *51*, 978–984. [[CrossRef](#)]
20. Creber, M.L.; Orrell, K.G.; Osborne, A.G.; Šik, V.; Hursthouse, M.B.; Light, M.E. Solution fluxionality of some pyridine-2,6-dialdehydes, -diketones and -diesters when acting as bidentate ligands in rhenium(I) and platinum(IV) complexes. Crystal structure of $[\text{ReBr}(\text{CO})_3\text{L}]$ ($\text{L} = \text{methylethyldipicolinate}$). *Polyhedron* **2001**, *20*, 1973–1982. [[CrossRef](#)]
21. Goher, M.A.; Mautner, F.; Hafez, A.K.; Youssef, A. Synthesis and characterization of copper(I) complexes of dimethyldipicolinate (dmdp) and X-ray structure of the mononuclear six-coordinate complex $[\text{Cu}(\text{dmdp})_2]\text{ClO}_4$. *Polyhedron* **2003**, *22*, 515–520. [[CrossRef](#)]
22. Kapoor, P.; Pathak, A.; Kapoor, R.; Venugopalan, P.; Corbella, M.; Rodríguez, M.; Robles, J.; Llobet, A. Structural, Electronic, and Magnetic Consequences of O-Carbonyl vs O-Alkoxy Ester Coordination in New Dicopper Complexes Containing the $\text{Cu}_2(\mu\text{-Cl})_2$ Core. *Inorg. Chem.* **2002**, *41*, 6153–6160. [[CrossRef](#)]
23. Platas-Iglesias, C.; Piguet, C.; André, N.; Bünzli, J.-C.G. Lanthanide triple-stranded helical complexes with a substituted 2,6-pyridinedicarboxylate. *J. Chem. Soc. Dalton Trans.* **2001**, 3084–3091. [[CrossRef](#)]
24. Muller, G.; Schmidt, B.; Jiricek, J.; Hopfgartner, G.; Riehl, J.P.; Bünzli, J.-C.G.; Piguet, C. Lanthanide triple helical complexes with a chiral ligand derived from 2,6-pyridinedicarboxylic acid. *J. Chem. Soc. Dalton Trans.* **2001**, 2655–2662. [[CrossRef](#)]
25. Renaud, F.; Piguet, C.; Bernardinelli, G.; Bünzli, J.-C.G.; Hopfgartner, G. In Search for Mononuclear Helical Lanthanide Building Blocks with Predetermined Properties: Lanthanide Complexes with Diethyl Pyridine-2,6-Dicarboxylate. *Chem. Eur. J.* **1997**, *3*, 1660–1667. [[CrossRef](#)]
26. Espinet, P.; García-Orodea, E.; Miguel, J.A. Mesogenic Palladium Complexes with Pincer Ligands Derived from Dipicolinic Acid. *Inorg. Chem.* **2000**, *39*, 3645–3651. [[CrossRef](#)] [[PubMed](#)]

27. Rasshoffer, W.; Müller, V.M.; Vögtle, F. Noncyclic Crown Ether Type Esters and Their Complexes. *Chem. Ber.* **1979**, *112*, 2095–2119.
28. Kirillov, A.M.; Haukka, M.; Da Silva, M.F.C.G.; Pombeiro, A.J.L. Synthesis, Characterization and Redox Behaviour of Mono- and Dicarbonyl Phosphane Rhenium(I) Complexes Bearing N-, N,N- and N,O-Type Ligands. *Eur. J. Inorg. Chem.* **2007**, *2007*, 1556–1565. [[CrossRef](#)]
29. Senegas, J.-M.; Bernardinelli, G.; Imbert, D.; Bünzli, J.-C.G.; Morgantini, P.-Y.; Weber, J.; Piguet, C. Connecting Terminal Carboxylate Groups in Nine-Coordinate Lanthanide Podates: Consequences on the Thermodynamic, Structural, Electronic, and Photophysical Properties. *Inorg. Chem.* **2003**, *42*, 4680–4695. [[CrossRef](#)]
30. Bogdan, N.; Grosu, I.; Benoît, G.; Toupet, L.; Ramondenc, Y.; Condamine, E.; Silaghi-Dumitrescu, I.; Plé, G. Molecular Rotors: Design, Synthesis, Structural Analysis, and Silver Complex of New [7.7]Cyclophanes. *Org. Lett.* **2006**, *12*, 2619–2622. [[CrossRef](#)]
31. Weng, Z.; Teo, S.; Hor, T.S.A. Metal Unsaturation and Ligand Hemilability in Suzuki Coupling. *Acc. Chem. Res.* **2007**, *40*, 676–684. [[CrossRef](#)] [[PubMed](#)]
32. Demerseman, B.; Toupet, L. Enolate-Phosphane Ligands Providing a Tool for the Selective Substitution of Triphenylphosphane by Carbon Monoxide or Trimethylphosphane in Complex {Ru(Cp)[η^2 -P,O-Ph₂PCH₂C(*t*Bu)=O](PPh₃)}[PF₆], and Subsequent Reactivity Towards Terminal Alkynes. *Eur. J. Inorg. Chem.* **2006**, *2006*, 1573–1581. [[CrossRef](#)]
33. Saes, B.W.H.; Verhoeven, D.G.A.; Lutz, M.; Gebbink, R.J.M.K.; Moret, M.-E. Coordination of a Diphosphine–Ketone Ligand to Ni(0), Ni(I), and Ni(II): Reduction-Induced Coordination. *Organometallics* **2015**, *34*, 2710–2713. [[CrossRef](#)]
34. Weber, B.; Werner, H. Osmium(II) and Osmium(IV) Complexes with Phosphane–Ethers, –Esters, and –Amines as Mono- and Bidentate Ligands. *Eur. J. Inorg. Chem.* **2007**, *2007*, 2072–2082. [[CrossRef](#)]
35. Mecking, S.; Keim, W. Cationic Palladium η^3 -Allyl Complexes with Hemilabile P,O-Ligands: Synthesis and Reactivity. Insertion of Ethylene into the Pd–Allyl Function. *Organometallics* **1996**, *15*, 2650–2656. [[CrossRef](#)]
36. Sileo, E.E.; Quinteros-Rivero, M.F.; Rivero, B.E.; Rigotti, G.; Blesa, M.A. Structure and reactivity of copper(II) carboxylates I. Copper(II) dipicolinates. *Solid State Ionics* **1994**, *73*, 153–159. [[CrossRef](#)]
37. Cingi, M.B.; Villa, A.C.; Gastini, C.; Nardelli, M. Crystal and molecular structures of divalent metal-complexes with pyridinecarboxylic acids. II. (Pyridine-2,6-dicarboxylato)diaquocopper(II), [Cu(C₇H₃NO₄)(OH₂)₂]. *Gazz. Chim. Ital.* **1971**, *101*, 825–832.
38. Glowiak, T.; Podgórska, I. X-ray, Spectroscopic and Magnetic Studies of Hexaaquacopper(II) Di(diphenylphosphate) Diglycine. *Inorg. Chim. Acta* **1986**, *125*, 83–88. [[CrossRef](#)]
39. Kirillova, M.V.; da Silva, M.F.C.G.; Kirillov, A.M.; da Silva, J.J.R.F.; Pombeiro, A.J.L. 3D hydrogen bonded heteronuclear Co^{II}, Ni^{II}, Cu^{II} and Zn^{II} aqua complexes derived from dipicolinic acid. *Inorg. Chim. Acta* **2007**, *360*, 506–512. [[CrossRef](#)]
40. Yue, C.; Lin, Z.; Chen, L.; Jiang, F.; Hong, M. The 2D–3D networks with infinite channels or difform chains of copper(II) complexes via weak non-covalent interactions. *J. Mol. Struct.* **2005**, *779*, 16–22. [[CrossRef](#)]
41. Wang, W.-Z.; Liu, X.; Liao, D.-Z.; Jiang, Z.-H.; Yan, S.-P.; Wang, G.-L. A novel one-dimensional, ferromagnetic copper(II) complex with chloro-bridges and hydrogen bonds: [(PDA)₂Cu₂(μ -Cl)₂][CuPz₂(H₂O)₄] (H₂PDA = pyridine-2,6-dicarboxylic acid, Pz = pyrazole). *Inorg. Chem. Commun.* **2001**, *4*, 327–331. [[CrossRef](#)]
42. Steiner, T. The Hydrogen Bond in the Solid State. *Angew. Chem. Int. Ed.* **2002**, *41*, 48–76. [[CrossRef](#)]
43. Powell, B.J.; Baruah, T.; Bernstein, N.; Brake, K.; McKenzie, R.H.; Meredith, P.; Pederson, M.R. A first-principles density-functional calculation of the electronic and vibrational structure of the key melanin monomers. *J. Chem. Phys.* **2004**, *120*, 8608–8615. [[CrossRef](#)]
44. Gussoni, M.; Castiglioni, C. Infrared intensities. Use of the CH-stretching band intensity as a tool for evaluating the acidity of hydrogen atoms in hydrocarbons. *J. Mol. Struct.* **2000**, *521*, 1–18. [[CrossRef](#)]
45. Brehm, M.; Kirchner, B. TRAVIS—A Free Analyzer and Visualizer for Monte Carlo and Molecular Dynamics Trajectories. *J. Chem. Inf. Model.* **2011**, *51*, 2007–2023. [[CrossRef](#)] [[PubMed](#)]
46. Klein, A.; Butsch, K.; Elmas, S.; Biewer, C.; Heift, D.; Nitsche, S.; Schlipf, I.; Bertagnolli, H. Oxido-pincer complexes of copper(II)—An EXAFS and EPR study of mono- and binuclear [(pydotH₂)CuCl₂]_n (*n* = 1 or 2). *Polyhedron* **2012**, *31*, 649–656. [[CrossRef](#)]
47. Halcrow, M.A. Jahn-Teller Distortions in Transition Metal Compounds, and Their Importance in Functional Molecular and Inorganic Materials. *Chem. Soc. Rev.* **2013**, *42*, 1784–1795. [[CrossRef](#)]

48. Hathaway, B.; Billing, D. The electronic properties and stereochemistry of mono-nuclear complexes of the copper(II) ion. *Coord. Chem. Rev.* **1970**, *5*, 143–207. [[CrossRef](#)]
49. Koval, I.A.; Sgobba, M.; Huisman, M.; Lüken, M.; Saint-Aman, E.; Gamez, P.; Krebs, B.; Reedijk, J. A remarkable anion effect on the crystal packing of two analogous copper complexes from a thiophene-containing phenol-based ligand. *Inorg. Chim. Acta* **2006**, *359*, 4071–4078. [[CrossRef](#)]
50. Thakurta, S.; Roy, P.; Rosair, G.; Gómez-García, C.J.; Garribba, E.; Mitra, S. Ferromagnetic exchange coupling in a new bis(μ -chloro)-bridged copper(II) Schiff base complex: Synthesis, structure, magnetic properties and catalytic oxidation of cycloalkanes. *Polyhedron* **2009**, *28*, 695–702. [[CrossRef](#)]
51. Yraola, F.; Albericio, F.; Corbella, M.; Royo, M. $[[\text{Cu}(\text{pzPh})(\text{Opo})]_2(\mu\text{-Cl})_2]$: A new dinuclear copper(II) complex with a chloride bridge and mixed blocking ligands. *Inorg. Chim. Acta* **2008**, *361*, 2455–2461. [[CrossRef](#)]
52. Pérez, A.L.; Neuman, N.I.; Baggio, R.; Ramos, C.A.; Dalosto, S.D.; Rizzi, A.C.; Brondino, C.D. Exchange interaction between $S = 1/2$ centers bridged by multiple noncovalent interactions: Contribution of the individual chemical pathways to the magnetic coupling. *Polyhedron* **2017**, *123*, 404–410. [[CrossRef](#)]
53. Rieger, P.H. *Electron Spin Resonance—Analysis and Interpretation*; RCS Publishing: Cambridge, UK, 2007.
54. Klein, A.; Elmas, S.; Butsch, K. Oxido Pincer Ligands—Exploring the Coordination Chemistry of Bis(hydroxymethyl)pyridine Ligands for the Late Transition Metals. *Eur. J. Inorg. Chem.* **2009**, *2009*, 2271–2281. [[CrossRef](#)]
55. Kaim, W.; Fiedler, J. Spectroelectrochemistry: The best of two worlds. *Chem. Soc. Rev.* **2009**, *38*, 3373. [[CrossRef](#)]
56. Kaim, W.; Klein, A. *Spectroelectrochemistry*; RSC Publishing: Cambridge, UK, 2008.
57. Sheldrick, G.M. A short history of SHELX. *Acta Crystallogr. Sect. A Found. Crystallogr.* **2008**, *64*, 112–122. [[CrossRef](#)] [[PubMed](#)]
58. Sheldrick, G.M. *SHELX-97, Programs for Crystal Structure Analysis*; University of Göttingen: Göttingen, Germany, 1997.
59. Farrugia, L.J. WinGX and ORTEP for Windows: An update. *J. Appl. Crystallogr.* **2012**, *45*, 849–854. [[CrossRef](#)]
60. Sheldrick, G.M. *SHELXL-2017/1, Program for the Solution of Crystal Structures*; University of Göttingen: Göttingen, Germany, 2017.
61. Sheldrick, G.M. Crystal structure refinement with SHELXL. *Acta Crystallogr. Sect. C Struct. Chem.* **2015**, *71*, 3–8. [[CrossRef](#)]
62. STOE X-RED. *Data Reduction Program, Version 1.22/Windows*; STOE & Cie: Darmstadt, Germany, 2001.
63. STOE X-SHAPE. *Crystal Optimisation for Numerical Absorption Correction, Version 1.06/Windows*; STOE & Cie: Darmstadt, Germany, 1999.
64. Horn, H.; Schäfer, A.; Ahlrichs, R. Fully optimized contracted Gaussian basis sets for atoms Li to Kr. *J. Chem. Phys.* **1992**, *97*, 2571–2577.
65. Lee, C.; Yang, W.; Parr, R.G. Development of the Colle-Salvetti correlation-energy formula into a functional of the electron density. *Phys. Rev. B* **1988**, *37*, 785–789. [[CrossRef](#)]
66. Becke, A.D. A new mixing of Hartree–Fock and local density-functional theories. *J. Chem. Phys.* **1993**, *98*, 1372–1377. [[CrossRef](#)]
67. Becke, A.D. Density-functional thermochemistry. III. The role of exact exchange. *J. Chem. Phys.* **1993**, *98*, 5648–5652. [[CrossRef](#)]
68. *TURBOMOLE 7.0*; TURBOMOLE GmbH: Karlsruhe, Germany, 2015.
69. Steffen, C.; Thomas, K.; Huniar, U.; Hellweg, A.; Rubner, O.; Schroer, A. TmoleX-A graphical user interface for TURBOMOLE. *J. Comput. Chem.* **2010**, *31*, 2967–2970. [[CrossRef](#)]
70. Frisch, M.J.; Trucks, G.W.; Schlegel, H.B.; Scuseria, G.E.; Robb, M.A.; Cheeseman, J.R.; Scalmani, G.; Barone, V.; Mennucci, B.; Petersson, G.A.; et al. *Gaussian 09*; Gaussian Inc.: Wallingford, CT, USA, 2009.
71. Hess, B.; Kutzner, C.; Van Der Spoel, D.; Lindahl, E. GROMACS 4: Algorithms for Highly Efficient, Load-Balanced, and Scalable Molecular Simulation. *J. Chem. Theory Comput.* **2008**, *4*, 435–447. [[CrossRef](#)] [[PubMed](#)]
72. Lemkul, J.A.; Allen, W.J.; Bevan, D.R. Practical Considerations for Building GROMOS-Compatible Small-Molecule Topologies. *J. Chem. Inf. Model.* **2010**, *50*, 2221–2235. [[CrossRef](#)] [[PubMed](#)]

73. Berendsen, H.J.; Postma, J.V.; van Gunsteren, W.F.; DiNola, A.R.H.J.; Haak, J.R. Molecular Dynamics with Coupling to an External Bath. *J. Chem. Phys.* **1984**, *81*, 3684–3690. [[CrossRef](#)]
74. Essmann, U.; Perera, L.; Berkowitz, M.L.; Darden, T.; Lee, H.; Pedersen, L.G. A Smooth Particle Mesh Ewald Method. *J. Chem. Phys.* **1995**, *103*, 8577–8593. [[CrossRef](#)]



© 2019 by the authors. Licensee MDPI, Basel, Switzerland. This article is an open access article distributed under the terms and conditions of the Creative Commons Attribution (CC BY) license (<http://creativecommons.org/licenses/by/4.0/>).